MOEM

Modern Electronic Materials 2022; 8(1): 43–50
DOI 10.3897/j.moem.8.1.84257

Research Article

Application of X-ray diffraction and reflectometry methods for analysis of damaged layers on polar faces of ZnO after surface chemical-mechanical treatment

Kirill D. Shcherbachev[1,2], Marina I. Voronova[2]

1 XRD Eigenmann GmbH, 6 Felsenweg, Schnaittach-Hormersdorf 91222, Germany

2 National University of Science and Technology MISiS, 4-1 Leninsky Ave., Moscow 119049, Russia

Corresponding author: Marina I. Voronova (mvoron@bk.ru)

Received 30 March 2022 ♦ **Accepted** 10 April 2022 ♦ **Published** 12 April 2022

Citation: Shcherbachev KD, Voronova MI (2022) Application of X-ray diffraction and reflectometry methods for analysis of damaged layers on polar faces of ZnO after surface chemical-mechanical treatment. *Modern Electronic Materials* 8(1): 43–50. https://doi.org/10.3897/j.moem.8.1.84257

Abstract

ZnO single crystals are used for the fabrication of laser targets for high-energy electron irradiated UV laser cathode-ray tubes and homoepitaxial substrates for lasers. The technology of ZnO based UV LEDs imposes strict requirements to surface quality. Chemical-mechanical polishing delivers good surface quality but it is known that polishing of ZnO polar faces may yield different results. Surface-sensitive high-resolution X-ray diffraction (HRXRD) and X-ray reflectometry (XRR) methods have been used for studying the structure of (0001) and $(000\bar{1})$ polar faces of ZnO after chemical-mechanical polishing. Two double-sided polished (0001) ZnO substrates have been cut out from different hydrothermally grown ingots. The damage and density depth profiles for the Zn and O faces of the specimens have been retrieved from the X-ray diffraction curves and the specular reflection curves, respectively. Intensity distributions in the vicinity of the [0002] and [0000] reciprocal lattice sites have been taken on a D8 Discover X-ray diffractometer (Bruker-AXS, Germany) in a triple-crystal setup. For separating the coherent and incoherent scattering components, the intensity profiles have been analyzed along sections perpendicular to the diffraction vector and located at different distances from the reciprocal lattice sites. The HRXRD and XRR data have been compared with atomic force microscopy (AFM) data. The HRXRD method has revealed damaged layers at both faces of the specimens, with the layer thicknesses differing for the Zn and O faces, i.e., 5–7 nm for the Zn face and 10–11 nm for the O face. The XRR method has shown that both faces are sufficiently smooth. These results have been confirmed by AFM (RMS roughness ~ 0.23±0.07 nm). However, the concentration of electrons in the superficial layers has been found to change. The layer thickness proves to be greater for the O face. We have hypothesized that the phenomena observed are caused by the difference in the chemical interaction of the Zn and O faces with the polishing agents.

Keywords

zinc oxide, laser targets, surface, lattice.

1. Introduction

Semiconductor electronics, optoelectronics and other fields of solid state electronic engineering are based on the use of semiconductor materials, dielectrics and metals, e.g. silicon multilevel VLICs, heterolasers, laser cathode-ray tubes **(CRT)** etc. Most devices are fabricated on complex epitaxial film structures grown on single crystal

substrates. Substrate surface preparation is an indispensable and complex stage of the design and batch fabrication of different-purpose electronic devices.

Finishing treatment of ZnO single crystals is required for the fabrication of laser targets for high-energy electron irradiated UV laser cathode-ray tubes and homoepitaxial substrates for lasers. A feature of II-VI semiconductor laser target operation is that efficient electron beam energy conversion to light occurs at a depth of less than 10 μm from single crystal laser target surface. Therefore there is the requirement to obtain perfect laser target surface having a roughness of within 1÷2 nm and a planarity of <5 N for a 50 mm diameter and a 5–20 μm thickness without micro- and macrodefects.

Zinc oxide **(ZnO)** is of interest as a transparent, conducting and cheap electrode material and a potential alternative to indium and tin oxide **(ITO)** in organic optoelectronic devices [1–4]. Unlike ITO, ZnO also provides the possibility of obtaining atomically smooth surfaces thus allowing the study of charge transfer processes in ZnO / organic semiconductor **(OSC)** heterojunctions with a clear interface geometry and energetic diagram.

ZnO substrates cut out perpendicularly to the growth direction [0001] have polar opposite faces due to the ZnO crystalline structure. Zn and O atomic layers interchange along the [1000] direction (Fig. 1). Chemical-mechanical polishing **(CMP)** for smooth surface treatment has different rates for the Zn and O faces. Under optimum conditions the Zn and O face etching rates were reported to be 0.2 and 0.02 μm/min, respectively [5]. The different etching responses of the anion and the cation faces are caused by a large ionic component in the chemical bonds: an increase in the ionic bond component leads to a greater difference between the etching rates for the A and B faces. The etchant and the ZnO reaction products have different adsorption parameters on different surfaces and affect the respective surface textures in different manners. The ZnO chalcogenide surface is more chemically active and more susceptible to the formation of complex colloidal compounds upon dissolution which do not dissolve completely and are adsorbed on the surface to form amorphous layers. The difficultly soluble complexes cause lower etching rates.

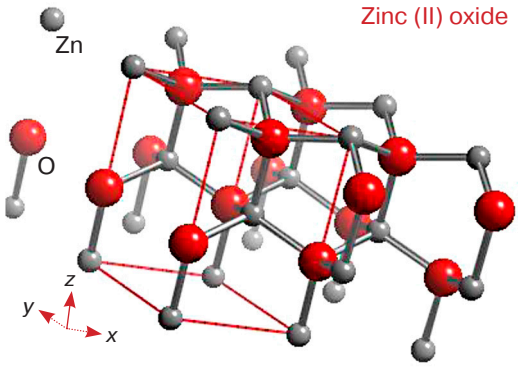

Figure 1. Layered crystalline structure of ZnO.

The aim of this work is to demonstrate the possibilities of the X-ray reflectometry (XRR) and high-resolution X-ray diffraction (HRXRD) methods in the resolution of structural differences between the polar faces of ZnO after CMP with compositions of amorphous colloidal silica, and to study the structure of the damaged surface layer of the wafers.

2. Experimental

The test specimens were two double-sided polished (0001) ZnO substrates 10 × 10 × 0.5 mm^3 in size cut out from different hydrothermally grown ingots. The ZnO substrates had a light-green color and were not heat treated either before or after polishing. The impurity content in hydrothermally grown crystals is on the order of 10^{-2}–10^{-3} wt.% [6]. Successful application of these substrates for the production of high-quality homoepitaxial ZnO films was demonstrated [7].

The X-ray diffraction study was carried out at the Joint Use Center for Materials Science and Metallurgy of National University of Science and Technology MISiS on a D8 Discover multipurpose X-ray diffractometer (Bruker-AXS, Germany) using the X-ray reflectometry **(XRR)** and high-resolution X-ray diffraction **(HRXRD)** methods. The X-ray source was a 1.6 kW copper anode X-ray tube. A parallel beam was formed with a Goebel mirror. Reflectometry study was conducted in a low-resolution setup. The X-ray beam divergence angle in this setup was 0.03°. For a high-resolution setup, the Cu$K_{\alpha 1}$ radiation component was cut out with a four-fold (n; $+n$) Ge(220) Bartels monochromator. The instrumental function width for this setup was 12".

The surface roughness of the specimens was measured with atomic force microscopy **(AFM)** on an MFP-3D Stand Alone instrument (Asylum Research, US) in the topography setup with an Asyelec-01 cantilever having a 120 kHz resonance frequency and rigidity k = 2 N/m. The typical scanning area was 2 × 2 μm^2, the scanning frequency being 0.8 Hz. The images were analyzed with the Gwyddion software (www.gwyddion.com).

The damage depth profiles for the Zn and O faces of the specimens were retrieved from the HRXRD diffraction curves [8]. The intensity distribution in the vicinity of the [0002] reciprocal lattice site was analyzed in a triple-axis setup. To separate the coherent and incoherent scattering components, the intensity profiles were analyzed along sections perpendicular to the diffraction vector and located at different distances from the [0002] reciprocal lattice site. The earlier described procedure [9] which is used for the analysis of the reciprocal space map **(RSM)** is based on the following assumptions regarding diffraction intensity distribution along $\mathbf{q_x}$ ($\mathbf{q}$ is the vector describing the deviation of the diffraction vector $\mathbf{Q}$ from the reciprocal lattice vector, $\mathbf{q_x}$ is the deviation vector

component parallel to the specimen surface and the wave vector length $|\mathbf{K}| = (2\pi/\lambda)$, where λ is the X-ray radiation wavelength):

– the presumed coherent peak is not bell-shaped meaning that there is no scatter due to mosaic or grained pattern;

– the full width at half maximum **(FWHM)** of the diffuse component of the peak is greater (by 2 or more times) than the width of the coherent scattering component. The halfwidth of the coherent peak should be comparable with the width of the instrumental function of the diffractometer (~12") and almost equal to that in the $\mathbf{q_z}$ direction ($\mathbf{q_z}$ is the deviation vector component perpendicular to the specimen surface);

– the coherent scattering intensity I_{coh} decreases following the law $I \sim q^{-n}$ for $n > 5$, whereas the diffuse scattering intensity I_{diff} decreases far less rapidly at $1 < n < 4$.

These assumptions being accepted, each RSM q-section can be considered as a sum of two bell-shaped functions with different intensity reduction rates:

$$I(q_x) = I_{coh}(q_x) + I_{diff}(q_x) + bkgr = \\ = \frac{A_1}{1+\left(\frac{q_x - \Delta_1}{hw_1}\right)^{n_1}} + \frac{A_2}{1+\left(\frac{q_x - \Delta_2}{hw_2}\right)^{n_2}} + bkgr,$$

where A_i is the maximum peak intensity ($i = 1, 2$); hw_i is the FWHM of the respective diffraction peak, n_i is the intensity reduction rate, Δ_i is the deviation from $q_x = 0$ for the coherent and the diffuse components, respectively, and *bkgr* is the constant intensity component due to detector noise.

The specimens were oriented so the $\mathbf{q_z}$ direction is parallel to the normal to the specimen, and hence the parameter $\Delta_i = 0$. Separation of the coherent and X-ray components of the experimental RSM requires sequential analysis of each q-section with the use of an optimization procedure.

The approach used for studying the structural damage in the specimens is typical for the retrieval of deformation and static Debye–Waller factor profiles in studies of ion implanted layers [8]. The diffraction curves were simulated on the basis of the dynamic diffraction theory. The damage depth profile is described with the static Debye–Waller factor profile $(\exp(-L_H))(z)$ which can be retrieved from the diffraction curve pattern. The L_H parameter depends on the RMS atom displacement $\langle u^2 \rangle$ from reciprocal lattice sites:

$$L_H = 8\,(\pi \sin\theta_B/\lambda)^2 \langle u^2 \rangle.$$

Then the Fourier components of polarizability in the damaged crystal can be rewritten as follows:

$$\chi_H = \chi_H^0 e^{-L_H}.$$

Since $0 < \exp(-L_H) \leq 1$, the introduction of a multiplier reduces the reflectivity of the damaged layer and hence reduces the diffracted wave amplitude proportionally to $|\chi_H^*|$. The wings of the diffraction peak are sensitive to the presence of a damaged layer. This approach allows one to control the quality of nanoscale-thickness surface layers.

The deformation and static Debye–Waller factor profile was set by an array of base points. The profile was simulated with a curve by connecting the points using the cubic spline interpolation method. Following that the resultant profile was split into 200 lamels. The thickness of each lamel depends on the full thickness of the damaged layer. For diffraction curve simulation, the positions of the base points of the deformation and static Debye–Waller factor profile were changed with a genetic algorithm based optimization software. This procedure provided for the best fit between the calculated and the experimental curves. The fit quality was assessed with the χ^2 criterion.

To obtain information about the electron density distribution over the depth of the damaged layer, two scans were measured by the XRR method in the vicinity of the ZnO(000) reciprocal lattice site. The first scan is a specular one for which the detector is rotated at an angular velocity two times that of the specimen. The **Q** vector is parallel to the normal to the surface because the incident and the reflected beams remain symmetrical to the surface. This scanning mode allows measuring the intensity distribution along the **Q** vector. There is contribution to scattering both from the electron density distribution and from the surface relief and the internal interfaces inside the damaged layer. The second scan is an offset one. For this scanning mode the angular velocity of detector rotation is also twice that of the specimen. However in the initial angular position the specimen is displaced by a small angle from the symmetrical specular position. Thus this scan is along a straight line, just like the specular scan, but tilted relative to the normal to the surface (or $\mathbf{Q_z}$).

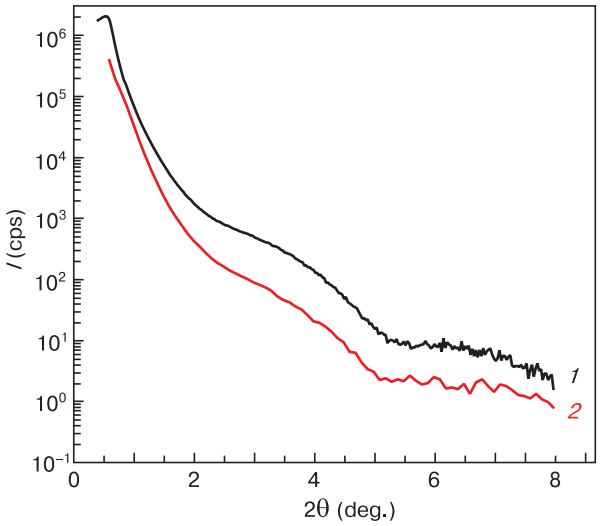

Figure 2. (*1*) Specular and (*2*) diffuse scattering distributions for Specimen 2 at the O face. Curve *2* is scanned with displacement $\Delta\omega = 0{,}1°$.

This scanning mode allows studying the distribution of scattering for $Q_x \neq 0$. The main contribution to scattering comes from diffuse scattering on surface roughness and internal interfaces.

Comparing the intensities for the two scans (Fig. 2) one can conclude about the main scattering mechanism, i.e., whether texture or electron density. For all the test specimens the main contribution to scattering comes from a gradual change of the electron density in the depth of the damaged layer.

Subtraction of the displacement scan curve from the specular scan curve yields a curve that can be described using Paratt's equations. This subtraction yielded an electron density depth profile in the damaged layer using the fitting procedure described earlier [10–12].

The fitting procedure is based on a trial-and-error method in which the experimental curve is compared with the calculated one until the best fit is achieved. Various functions can be accepted as the fitting criterion. Initially, a reflectometric curve is calculated based on the source parameters of the specimen. Then this curve is corrected by changing its parameters (layer thickness, roughness, boundary thickness and layer density) and experimental parameters (intensity, background), and a new curve is plotted. The procedure is repeated until any of the fitting procedure stop criteria is satisfied (the required fit between the calculated and the experimental curves is achieved, the preset maximum number of iterations is exceeded or it becomes impossible to reduce the value of the goal function that describes the fit criterion). In this work, the background level was determined by the diffuse scattering curve.

2.1. Density depth profile description

The coefficient of X-ray reflection from surface roughness was calculated using a model based on the representation of the interface roughness j as a series of smooth transition layers [13] the refraction index of which obeys the smooth function $n_j(z) = n_j + (n_{j+1} - n_j)F(z, \sigma_j)$, where z is the vertical coordinate of depth (perpendicular to the multilayered surface) and n_j, n_{j+1} are the refraction indices for the two media far from the interface. The refraction index of each transition layer k is assumed to be constant and equal to the refraction index of the middle point z_k of the transition layer, $n_j(z_k)$. The coupling function $F(z, \sigma_j)$ can be accepted to be linear [15], sinusoidal [16] or most often error function [17] as was the case in this work. For the error function (which corresponds to a Gaussian distribution of vertical roughness) the refraction index can be written as follows:

$$n_j(z) = \frac{n_j + n_{j+1}}{2} + \frac{n_j + n_{j-1}}{2} Erf\left(\frac{z}{\sqrt{2}\sigma_j}\right).$$

The transition layers method is the most precision way to simulate surface roughness and allows one to use any type of roughness distribution but it also requires far more time for calculations and is not typically used for the simulation of multilayered structures [18]. Correct choice of the minimum number of transition layers is important for correct simulation of their reflectivity.

2.2. Analysis of indeterminacy of resultant model parameters

The χ^2 parameter is used in statistical analysis not only as the optimization function for the assessment of optimization parameters but also as the statistic hypothesis verification criterion which allows one to assess the quality of fit or choose the optimum model if multiple spectrum description options are available.

$$\chi^2(\beta) = \frac{1}{n - n_p} \sum_{i=1}^{n} \frac{\left(I_i^E - I_i^T(\beta)\right)^2}{s_i^2}, \quad (1)$$

where s_i is the intensity measurement error I_i^E, n is the number of points in the curve and n_p is the number of model parameters measured (dimension of the optimization parameter vector β).

The accuracy of optimization parameter vector β determination can be assessed by plotting the inverse covariance matrix C_{kl}^{-1} (having the dimension $n_p \times n_p$) which is calculated at the optimization stage using the Marquardt–Levenberg method [19]:

$$C_{kl}^{-1} = \sum_{i=1}^{n} \frac{1}{s_i^2} \left[\frac{\partial I_i^T}{\partial \beta_k} \frac{\partial I_i^T}{\partial \beta_l}\right]\Bigg|_{\beta=\beta_0}, \quad (2)$$

where s_i is the intensity measurement error I_i^E, n is the number of points in the curve and β_0 is the parameter vector obtained upon the end of the optimization procedure. Then the standard error σ_i can be determined from the following relationship:

$$\sigma_i = \sqrt{C_{ii}\chi^2}, \quad (3)$$

where C_{ii} is the diagonal element of the covariance matrix.

Equation (1) contains the actual error at each specific point rather than some averaged statistical error for the entire diffraction curve. This allows one to take into account the different information values of different diffraction curve points. The points having the greatest intensity measurement errors have smaller effect on the values of the retrieved parameters. Since the reflection coefficient changes by several orders of magnitude in the experimental angular range, it is convenient to use the logarithmic scale for representing experimental data and assessing fit quality. Equation (1) can be rewritten for the logarithmic scale, but one will then have to take into account the change in the error value [20]:

$$\chi^2 = \frac{1}{n-n_p}\sum_{i=1}^{n}\frac{|\log I_i^E - \log I_i^T|}{s_i^2}, \quad (4)$$

where s_i is the relative intensity measurement error for each point. It was reported [21] that the logarithmic representation of error function is especially efficient for the analysis of spectra where the scatter of intensity values is several orders of magnitude (as is the case for high-resolution diffraction and XRR).

3. Results and discussion

Atomic force microscopy did not reveal any difference between the Zn and O faces of the test substrates. The RMS roughness of the specimens was within (0.30÷0.32) ± 0.07 nm.

However, XRR showed a reliable difference between the density depth profiles of the thin surface layers for the Zn and O faces. Figure 3 *a* and *c* shows the experimental reflectometric curves with superimposed curves calculated using the model density depth profiles as shown in Fig. 3 *b* and *d*.

The reflectometry curves for the different faces of the specimens differ in shape (Fig. 3 *a* and *c*). Hence there is a tangible difference between the density depth profiles of their surface layers (Fig. 3 *b* and *d*). The thickness of the variable density layer at the Zn face is less than 3 nm, whereas the layer at the O face is by at least 1 nm thicker.

Thus the XRR method showed its high sensitivity to surface layer density after CMP. However, this method cannot sense changes in the material's crystalline structure. The degree of damage in the crystalline structure was assessed using the HRXRD method.

We separated the coherent scattering component using the coherent and incoherent diffuse scattering separation procedure. The wings of the profile for this component should exhibit a quadratic law of scattering intensity decrease. The presence of defects in the vicinity of the surface causes a steeper decline in the scattering intensity (Fig. 4 *a*). The difference between the scattering intensity decrease rate at the wings of the

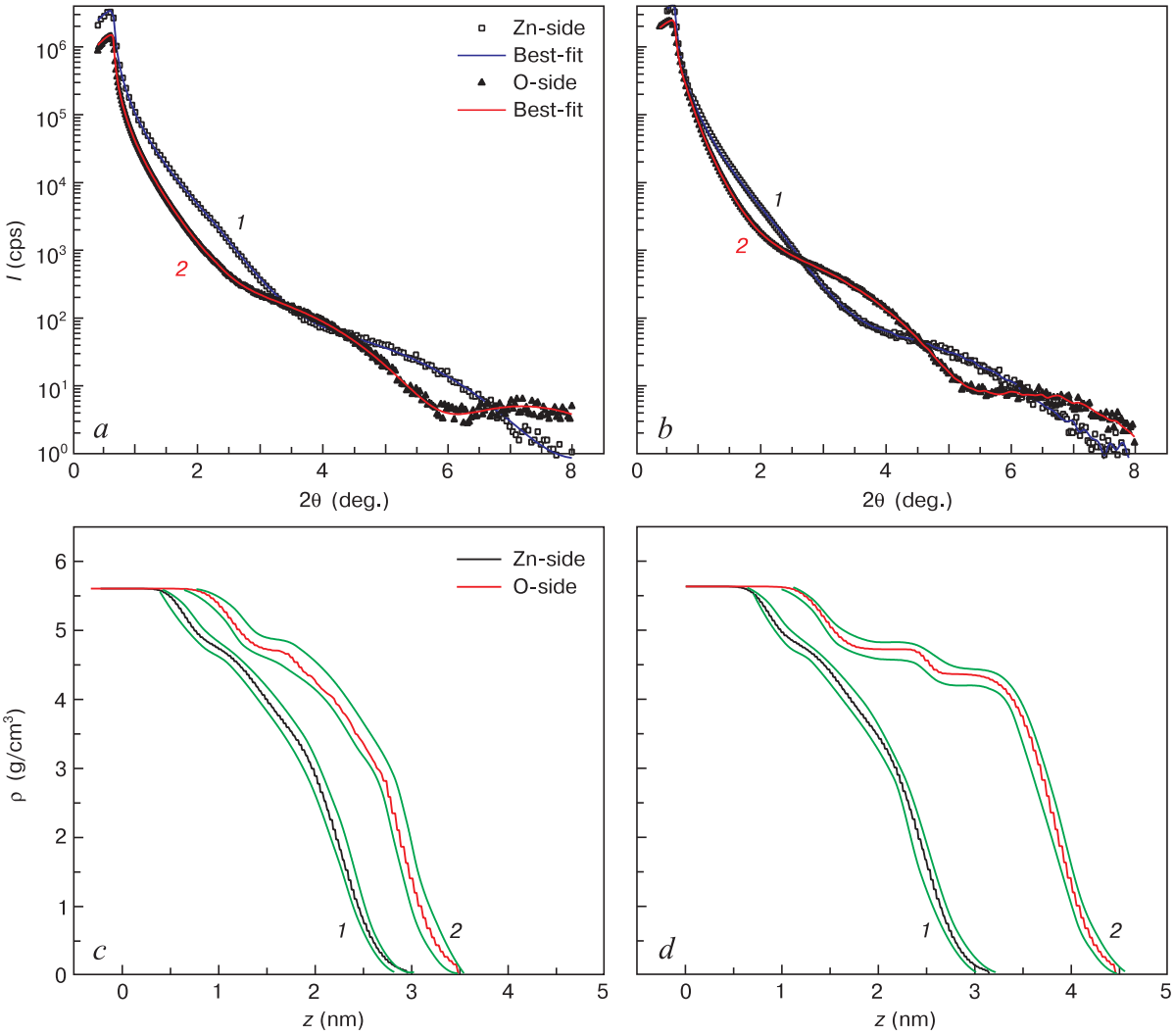

Figure 3. (*a* and *c*) Experimental and calculated reflectometric curves and density depth profiles for damaged layer *z* and (*b* and *d*) their confidence ranges $\Delta\chi^2 = 3$ for (*1*) Zn and (*2*) O faces of Specimens 1 and 2, respectively.

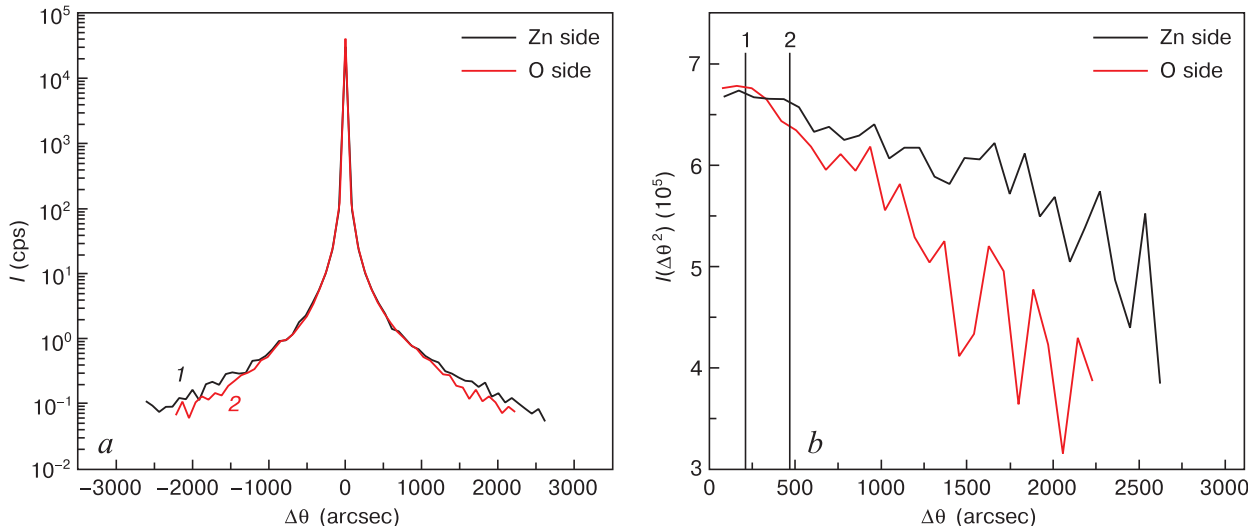

Figure 4. (*a*) Diffraction curves for Specimen 1 and (*b*) normalized diffraction intensity *vs* angular deviation from reciprocal lattice site ZnO(0002): (*a*): *1* and *2*: Zn and O faces, respectively; (*b*): *1* and *2*: angular deviation from reciprocal lattice site at which intensity starts decreasing steeper than $I \sim \Delta\theta^{-2}$ for Zn and O faces, respectively.

diffraction curve is more expressed if the normalized intensity is plotted *vs* angular deviation from the exact Bragg position [22] (Fig. 4 *b*).

The thickness of the damaged layer *i* can be assessed within the kinematic diffraction theory [22]:

$$l = \frac{\lambda}{4\pi\Delta\theta\cos\theta_B},$$

where λ is the X-ray wavelength, θ_B is the Bragg angle for the ZnO(0002) reflection and Δθ is the angular deviation from the reciprocal lattice site at which intensity starts decreasing steeper than $I \sim \Delta\theta^{-2}$.

For Specimen 1, the estimate of the thickness *i* was 5 nm for the Zn face and 10 nm for the O face. For Specimen 2, these estimates were 6 and 12 nm, respectively.

The Debye–Waller depth profiles for the damaged layers of the test specimens were retrieved from the analysis of the diffraction curve (Fig. 5). For Specimen 1, the average damaged layer thickness was 5 nm for the Zn face and 10 nm for the O face. For Specimen 2, these estimates were 7 and 11 nm, respectively. The estimates based on the kinematic diffraction theory proved to be close to those obtained within the dynamic scattering theory. Thus, the HRXRD data also suggest that the thickness of the damaged layer at the Zn face is smaller than that at the O face.

For the treatise of the Debye–Waller depth profiles one should take into account that this experiment does not allow separating the single crystal / amorphous and the amorphous / polycrystal interfaces. In both cases $\exp(-L_H) \to 0$.

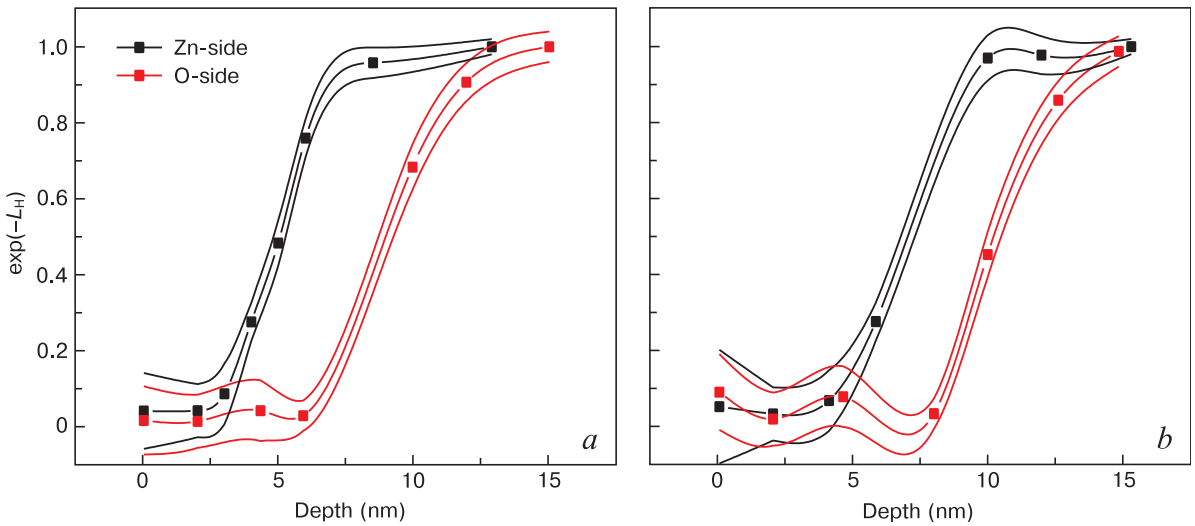

Figure 5. Debye–Waller depth profiles for the damaged layers at the Zn and O faces of Specimens (*a*) 1 and (*b*) 2. Thin curves mark the confidence ranges.

One can assume that poorly soluble products of chemical reactions of the etchant components with ZnO form layers with decreasing density on the wafer surface. These products are adsorbed differently at the Zn and O faces of the single crystal wafer surfaces and form amorphous layers of different thicknesses.

The difference between the etching parameters of the anion and cation faces of II-VI semiconductor compound wafers unlike III-V ones originates from a large ionic component in the chemical bonds: an increase in the ionic bond component leads to a greater difference between the etching rates for the A and B faces. The etchant and the ZnO reaction products have different adsorption parameters on different surfaces and affect the respective surface textures in different manners. The ZnO chalcogenide surface is more chemically active and more susceptible to the formation of complex colloidal compounds upon dissolution which do not dissolve completely and are adsorbed on the surface to form amorphous layers that are in turn detected by the XRR and HRXRD methods.

4. Conclusion

Combination of the XRR and HRXRD methods allows studying the structure of superficial layers at the Zn and O faces of (0001) ZnO substrates after double-sided CMP. Both methods reveal a statistically reliable difference between the thicknesses of the damaged layers forming at the polar faces of ZnO as a result of CMP. HRXRD showed the presence of damaged layers at both sides of the specimens, but the thicknesses of the layers were different: 5–7 nm for the Zn face and 10–11 for the O face. The transition layer thicknesses as assessed by XRR were 3 nm for the Zn faces and 3.5–4.5 nm for the O faces of the test substrates. AFM did not reveal any difference between the two sides. The RMS roughness was about 0.3 ± 0.07 nm. It is assumed that the observed phenomena originate from the different chemical interaction of the Zn and O surfaces with the polishing agents.

Acknowledgments

The work was carried out with financial support from the Ministry of Science and Higher Education of the Russian Federation within State Assignment (Fundamental Research Project No. 0718-2020-0031) on the equipment of the Joint Use Center for Materials Science and Metallurgy and with State financial support from the Ministry of Science and Higher Education, Grant No. 075-15-2021-696.

References

1. Minami T. Transparent conducting oxide semiconductors for transparent electrodes. *Semiconductor Science and Technology*. 2005; 20(4): S35. https://doi.org/10.1088/0268-1242/20/4/004
2. Bhosle V., Prater J.T., Yang F., Burk D., Forrest S.R., Narayan J. Gallium-doped zinc oxide films as transparent electrodes for organic solar cell applications. *Journal of Applied Physics*. 2007; 102(2): 023501–023501-5. https://doi.org/10.1063/1.2750410
3. Owen J., Son M.S., Yoo K.-H., Ahn B.D., Lee S.Y. Organic photovoltaic devices with Ga-doped ZnO electrode. *Applied Physics Letters*. 2007; 90(3): 033512. https://doi.org/10.1063/1.2432951
4. Kim Y.H., Kim J.S., Kim W.M., Seong T.-Y., Lee J., Müller-Meskamp L., Leo K. Realizing the potential of ZnO with alternative non-metallic co-dopants as electrode materials for small molecule optoelectronic devices. *Advanced Functional Materials*. 2013; 23(29): 3645–3652. https://doi.org/10.1002/adfm.201202799
5. Farafonov S.B. Chemical-mechanical polishing of ZnO, NiSb, Cu single crystals and cylindrical Si substrates. Diss. Cand. Sci. (Eng.). Moscow: NUST MISiS; 2011. 213 p. (In Russ.)
6. Kuzmina I.P., Nikitenko V.A. Zinc oxide. Preparation and optical properties. Moscow: Nauka; 1984. 166 p. (In Russ.)
7. Artemov A.S., Gorbatenko L.S., Novodvorsky O.A. , Sokolov V.I., Farafonov S.B., Khramova O.D. Preparation of ZnO and a-Al_2O_3 substrates for creating UV lasers. *Nanotechnology*. 2007; 4(12): 46–50. (In Russ.)
8. Shcherbachev K.D., Bublik V.T., Mordkovich V.N., Pazhin D.M. The influence of photoexcitation in situ on a generation of defect structure during ion implantation into Si substrates. *Journal of Physics D: Applied Physics*. 2005; 38(10A): A126. https://doi.org/10.1088/0022-3727/38/10a/024
9. Shalimov A., Shcherbachev K.D., Bak-Misiuk J., Misiuk A. Defect structure of silicon crystals implanted with H_2^+ ions. *Physica Status Solidi A: Applications and Materials*. 2007; 204(8): 2638–2644. https://doi.org/10.1002/pssa.200675697
10. Bowen D.K., Tanner B.K. X-ray metrology in semiconductor manufacturing. Boca Raton: CRC Press; 2006. 279 p. https://doi.org/10.1201/9781315222035
11. Holy V., Baumbach T. Non-specular X-ray reflection from rough multilayers. *Physical Review B*. 1994; 49(15): 10668–10676. https://doi.org/10.1103/physrevb.49.10668
12. ISO 16413:2020. Evaluation of thickness, density and interface width of thin films by X-ray reflectometry – Instrumental requirements, alignment and positioning, data collection, data analysis and reporting. Publ. 08.2020. https://www.iso.org/standard/76403.html
13. Croce R., Névot L. Étude des couches minces et des surfaces par réflexion rasante, spéculaire ou diffuse, de rayons X. *Revue de Physique Appliquée (Paris)*. 1976; 11(1): 113–125. https://doi.org/10.1051/rphysap:01976001101011300
14. Artioukov I.A., Asadchikov V.E., Kozhevnikov I.V. Effects of a near-surface transition layer on X-ray reflection and scattering. *Journal of X-Ray Science and Technology*. 1996; 6(3): 223–243. https://doi.org/10.3233/xst-1996-6301
15. Croce R., Névot L., Pardo B. Contribution a l'étude des couches minces par réflexion spéculaire de rayons X. *Nouvelle Revue d'Op-*

tique Appliquée. 1972; 3(1): 37–50. https://doi.org/10.1088/0029-4780/3/1/307

16. Underwood J.H., Barbee T.W. Layered synthetic microstructures as Bragg diffractors for X-rays and extreme ultraviolet: theory and predicted performance. *Applied Optics*.1981; 20(17): 3027–3034. https://doi.org/10.1364/ao.20.003027
17. Benediktovitch A., Feranchuk I., Ulyanenkov A. Theoretical concepts of X-ray nanoscale analysis. Theory and applications. Springer; 2014. 318 p. https://doi.org/10.1007/978-3-642-38177-5
18. Stoev K., Sakurai K. Recent theoretical models in grazing incidence X-ray reflectometry. *The Rigaku Journal*. 1997; 14(2): 22–37.
19. Press W.H., Teukolsky S.A., Vetterling W.T., Flannery B.P. Numerical Recipes in C. NY: Cambridge University Press; 1996. 994p.
20. Afanas'ev A.M., Chuev M.A., Imamov R.M., Lomov A.A., Mokerov V.G., Federov Yu.V., Guk A.V. Study of multilayer GaAs-$In_xGa_{1-x}As$/GaAs layer-based structure by double-crystal X-ray diffractometry. *Crystallography Reports*. 1997; 42(3): 467–476.
21. Wormington M., Panaccione C., Matney K.M., Bowen D.K. Characterization of structures from X-ray scattering data using genetic algorithms. *Philosophical Transactions of the Royal Society of London. Series A: Mathematical, Physical and Engineering Sciences*. 1999; 357: 2827. https://doi.org/10.1098/rsta.1999.0469
22. Afanasyev A.M., Alexandrov P.A., Imamov R.M. X-ray diffraction diagnostics of submicron layers. Moscow: Nauka; 1989. 152 p. (In Russ.)